Testing the *P/S* Amplitude Seismic Source Discriminant at Local Distances Using Seismic Events Within and Surrounding the Kloof Gold Mine, South Africa, and the Kiruna Iron Ore Mine, Northern Sweden

Sampath Rathnayaka*[1], Andrew Nyblade[1,2], Björn Lund[3], Charles Ammon[1], Raymond Durrheim[2], and Richard Masethe[2,4]

ABSTRACT

We investigate the utility of the *P/S* amplitude discriminant for small seismic events recorded at local distances on surface seismic networks using (1) mining-related events from within the Kloof gold mine in South Africa; and (2) mining-related events and earthquakes within and adjacent to the Kiruna iron ore mine in northern Sweden. For the Kloof mine, seventy-five source mechanisms characterized by moment tensor solutions obtained using high-frequency in-mine seismic data are used to evaluate three mine-related source types, isotropic (crush), compensated linear vector dipole (crush-slip), and double-couple (DC; pure slip). For the Kiruna mine region, 270 events are used to evaluate earthquake sources, chemical explosions, and mine-related seismic events (primarily isotropic). For the Kloof mine events, we find that average *P/S* amplitude ratios measured in the 2–6 Hz frequency band discriminate between isotropic and DC events, and if only pure-slip events with a DC component of > 60% are considered, the effective frequency band can be extended from 2 to 8 Hz. For the Kiruna region events, *P/S* amplitude ratios effectively discriminate earthquakes from chemical explosions in the 4–6 Hz and 10–28 Hz frequency bands. Our findings further show that average *P/S* amplitude ratios for mine-related events and earthquakes separate at frequencies of 10 Hz and higher. A comparison of amplitude ratios for crush and pure-slip events located within a depth range of 1 km in the Kloof mine, and a comparison of amplitude ratios of shallow (< 10 km depth) and deep-focus (> 20 km depth) earthquakes in the Kiruna region, indicate that the *P/S* amplitude discriminant is not influenced significantly by source depth. These findings thus suggest that the *P/S* amplitude discriminant, originally developed for larger events recorded at regional and teleseismic distances, can be extended to smaller events recorded at local distances.

KEY POINTS

- We investigated if average *P/S* amplitude ratios can be used to discriminate small (**M** < 4) seismic events.
- Results show that *P/S* ratios separate isotropic events from double-couple events for a range of frequencies.
- *P/S* amplitude ratios have the potential to discriminate small seismic sources recorded at local distances.

Supplemental Material

1. Department of Geosciences, Pennsylvania State University, University Park, Pennsylvania, U.S.A., https://orcid.org/0000-0001-9763-8358 (CA); 2. School of Geosciences, The University of the Witwatersrand, Johannesburg, South Africa, https://orcid.org/0000-0003-3832-0600 (RD); https://orcid.org/0000-0002-4420-7885 (RM); 3. Department of Earth Sciences, Uppsala University, Uppsala, Sweden, https://orcid.org/0000-0002-0789-5949 (BL); 4. Sibanye-Stillwater Ltd., Johannesburg, South Africa

*Corresponding author: scr5394@psu.edu

Cite this article as Rathnayaka, S., A. Nyblade, B. Lund, C. Ammon, R. Durrheim, and R. Masethe (2024). Testing the *P/S* Amplitude Seismic Source Discriminant at Local Distances Using Seismic Events Within and Surrounding the Kloof Gold Mine, South Africa, and the Kiruna Iron Ore Mine, Northern Sweden, *Bull. Seismol. Soc. Am.* **114**, 2237–2250, doi: 10.1785/0120230215

INTRODUCTION

The discrimination of seismic sources is an essential component of seismic monitoring, and with a growing interest in the testing of low-yield explosive devices comes an increased need to improve methodologies for discriminating small seismic event types (i.e., ~**M** < 4 events; e.g., Snelson *et al.*, 2013; Maceira *et al.*, 2017). For larger seismic events (i.e., ~**M** > 4) recorded at regional and teleseismic distances, amplitude ratios between *P* and *S* body waves have been widely and effectively used in source discrimination (e.g., Walter *et al.*, 1995; Taylor, 1996; Taylor *et al.*, 2002; Walter *et al.*, 2018). For example, Walter *et al.* (2018) showed that *P*- and *S*-wave amplitude ratios effectively separate explosions from earthquakes in the 2–4 Hz frequency range, whereas Taylor *et al.* (2002) showed for a different dataset that *P/S* amplitudes clearly separate explosions from earthquakes in the 4–8 Hz frequency range.

The efficacy of *P/S* amplitude ratios for discriminating small events, often well recorded only at local distances, however, remains a subject of investigation (e.g., Kim *et al.*, 1993, 1997; O'Rourke *et al.*, 2016; Pyle and Walter, 2019). In this study, we use two locally recorded datasets containing a range of **M** < 4 source types to evaluate the utility of the *P/S* amplitude discriminant. One dataset is from the Kloof gold mine in South Africa, hereafter referred to as the Kloof dataset, where mine seismic events classified using moment tensor (MT) solutions determined from high-frequency in-mine data (e.g., Sweby *et al.*, 2006; Masethe *et al.*, 2022, 2023) provide the "ground truth" against which we evaluate the *P/S* amplitude discriminant. The other dataset is from the Kiruna iron ore mine in northern Sweden and a nearby postglacial fault system, hereafter referred to as the Kiruna dataset, and contains mine blasts (chemical explosions), mining-related seismicity, and earthquakes.

It is well known that mine-related seismic events in the deep gold mines of South Africa include a wealth of source types displaying a continuous distribution between volumetric closure (i.e., nondouble-couple or pillar collapse) and normal faulting (i.e., double-couple [DC] or fault slip) mechanisms (McGarr, 1992; Julià *et al.*, 2009; Masethe, 2022; Masethe *et al.*, 2022, 2023). Hence, the gold mines provide a rich seismic environment for investigating the utility of *P/S* amplitude ratios for discriminating small seismic sources. Source mechanisms of mine seismic events are often classified using MT inversion solutions obtained using high-frequency (sampling at ~6 kHz) data from in-mine seismic stations typically located a few meters to several hundred meters from the source (e.g., Julià *et al.*, 2009; Mendecki, 2013; Masethe *et al.*, 2022, 2023). We use seismic data from 75 events in the Kloof gold mine recorded on surface stations at distances of <130 km. Masethe *et al.* (2023) computed MT solutions for the events using data from in-mine seismic networks. Fifty events are classified as double-couple (DC; pure-slip), 19 events as compensated linear vector dipole (CLVD; crush-slip), and six as isotropic (ISO; crush).

The Kiruna iron ore mine and the nearby (~40 km) postglacial Pärive fault system provides an equally rich seismic environment for investigating the utility of *P/S* amplitude ratios for small seismic source discrimination. Source types in the Kiruna iron ore mine include daily chemical explosions and hundreds of mining-related events. We use seismic data from 270 **M** < 4 events, which includes equal numbers (i.e., 90) of blasts and mine-related events recorded on surface stations at distances of < 200 km, and earthquakes from the Pärvie fault system recorded at distances of < 260 km.

The processing of the Kloof and Kiruna datasets follow the procedures described in Kintner *et al.* (2020). *P* and *S* amplitudes are calculated by taking the root mean square (rms) of the vertical (Z), radial (R), and transverse (T) components to ensure the inclusion of the full amplitude for each arrival, regardless of incident angles or polarization of the seismic wave. The maximum rms value among three components was obtained for each phase, and a correction is applied to remove site amplification and distance propagation effects on each measurement. If the *P/S* amplitude ratio discriminant behaves similarly for small events recorded at local distances compared with larger events recorded at regional and teleseismic distances (e.g., Walter *et al.*, 1995, 2018; Taylor, 1996; Taylor *et al.*, 2002), then a separation of the measured *P/S* amplitude ratios for the various source types in both the datasets should be evident, at least for some frequency bands.

BACKGROUND

Kloof mine

The Kloof Gold mine is located in the Carletonville mining district on the northern side of the Precambrian Witwatersrand Basin in northern South Africa (Coward *et al.*, 1995; Beach and Smith, 2007; Dankert and Hein, 2010; Fig. 1). The Witwatersrand Basin lies within the Archean Kaapvaal Craton and was formed between 3.7 and 2.7 Ga (Tankard *et al.*, 1982; Hunter *et al.*, 2006). Our data come from five seismic networks in the Johannesburg, Carletonville, and Klerksdorp mining regions (Fig. 1).

The geology in and surrounding the Kloof gold mine is shown in Figures S1 and S2, available in the supplemental material to this article. The basal Dominion Group is composed of volcano-sedimentary strata and is overlain by the Witwatersrand Supergroup, which can be divided into the West Rand Group and the Central Rand Group. The West Rand Group is mainly composed of quartzites and ferruginous shale, whereas the Central Rand Group consists mostly of quartzites (McCarthy, 2006; Dankert and Hein, 2010). The metabasaltic rock of the Ventersdorp Supergroup lies unconformably above the Witwatersrand Supergroup, whereas the Ventersdorp Contact Reef (VCR), a gold-bearing quartz pebble conglomerate and a main ore body, is sandwiched between them. The VCR ore body is ~1.5 m thick, strikes to the north-northeast, dips at 25° to the southeast, and lies at 1–4.2 km depth (Manzi *et al.*, 2014). The

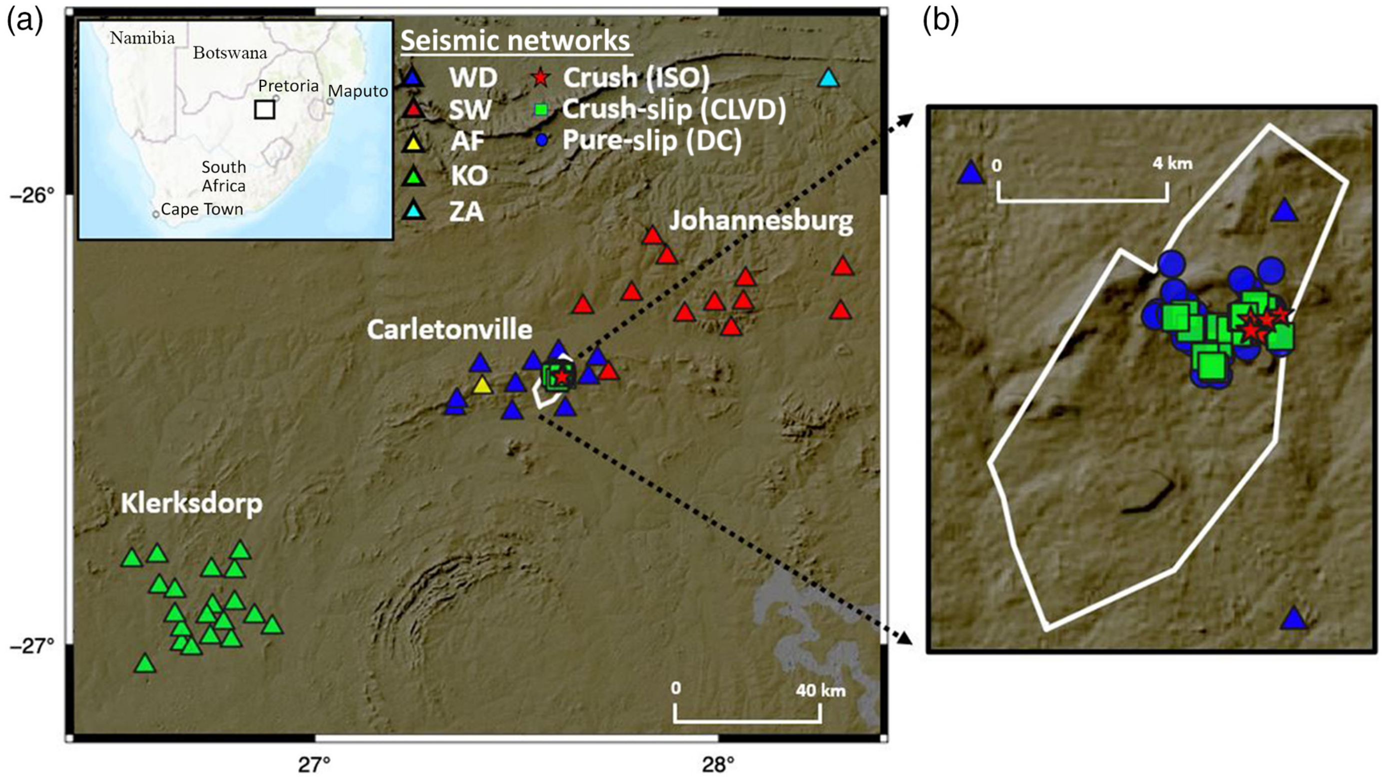

Figure 1. (a) The distribution of seismic stations and events in South Africa used in this study. The blue, red, green, cyan, and yellow triangles represent instruments from the Western Deep (WD) seismic network, the Strategic Water (SW) Management Project network, the seismic network in Klerksdorp–Orkney (KO) region, the South African National Seismograph network (ZA), and the Africa Array network (AF), respectively. The study area is shown by the small box in the inset map. (b) The white polygon outlines the Kloof gold mine. The red stars, green squares, and blue circles on the map show crush, crush-slip, and pure-slip event locations, respectively. The color version of this figure is available only in the electronic edition.

Transvaal Supergroup is mainly comprised of lava flows and alternating beds of quartzite, shale, siltstone, chert, and dolomites (Jones, 2003). The Triassic–Jurassic Karoo Supergroup, consisting of shales and sandstones, overlies the Transvaal Supergroup rocks at the top of the section. A significant portion of the Klerksdorp region is covered by poorly compacted and highly variable soils (e.g., clayey silty sand with gravels, boulders, ash layers, etc.), which are overlain by alluvial and/or colluvial soils (Diop *et al.*, 2016).

In the Kloof gold mine, crush-type (ISO) events are associated with tensile failure typically resulting from fracturing at excavation faces (Gibowicz and Kijko, 1994; Hudyma and Potvin, 2010; Masethe, 2022; Masethe *et al.*, 2022) or with pillar collapses from highly stressed rock volumes (Keneti and Sainsbury, 2018). Pure-slip (DC) events typically result from unstable slip or rupture along preexisting planes of weakness within the mine (Boatwright and Fletcher, 1984; Keneti and Sainsbury, 2018; Masethe, 2022; Masethe *et al.*, 2022), and crush-slip (CLVD) events result from a combination of tensile failure and shear slip (Boatwright and Fletcher, 1984; Gibowicz and Kijko, 1994; Masethe, 2022; Masethe *et al.*, 2022).

Kiruna mine

The Kiruna mining area is located in northern Sweden (Fig. 2) covering an area of 30 km^2 (Huber, 2023). The study area lies within the northwestern Fennoscandian Shield, close to the Caledonian front (Bayanova *et al.*, 2009; Ernst and Bleeker, 2010). The geology of the region (see Figs. S3 and S4) includes a rift related to about 2.3–2 Ga greenstone belt and Svecofennian (1960–1850 Ma) subduction-related igneous and sedimentary rocks laying unconformably on Archean basement (Martinsson, 2004; Martinsson *et al.*, 2013). The geology in and immediately surrounding the Kiruna mine includes a succession of greenstones, porphyries, and clastic sedimentary rocks, all resting unconformably on Archean basement. The ~2.5–2.1 Ga old Kovo and Kiruna greenstone groups are the lowest stratigraphic units in the area. The 1.9 Ga old Kurravaara conglomerate, Kiirunavaara Group, and Hauki quartzite are unconformably overlaid by Karelian-aged rocks. The Kiirunavaara (Kiruna) ore body trends ~4 km north to south reaches depths of up to 2 km, is on average ~80 m thick (Sievertsson, 2012), and dips 60°–70° to the east (Cliff *et al.*, 1990). The ore body is hosted within the Kiirunavaara Group, which includes mixed volcanic and sedimentary units composed of rhyolite, basalt, conglomerate, greywacke, and schist (Martinsson, 2004; Martinsson *et al.*, 2013).

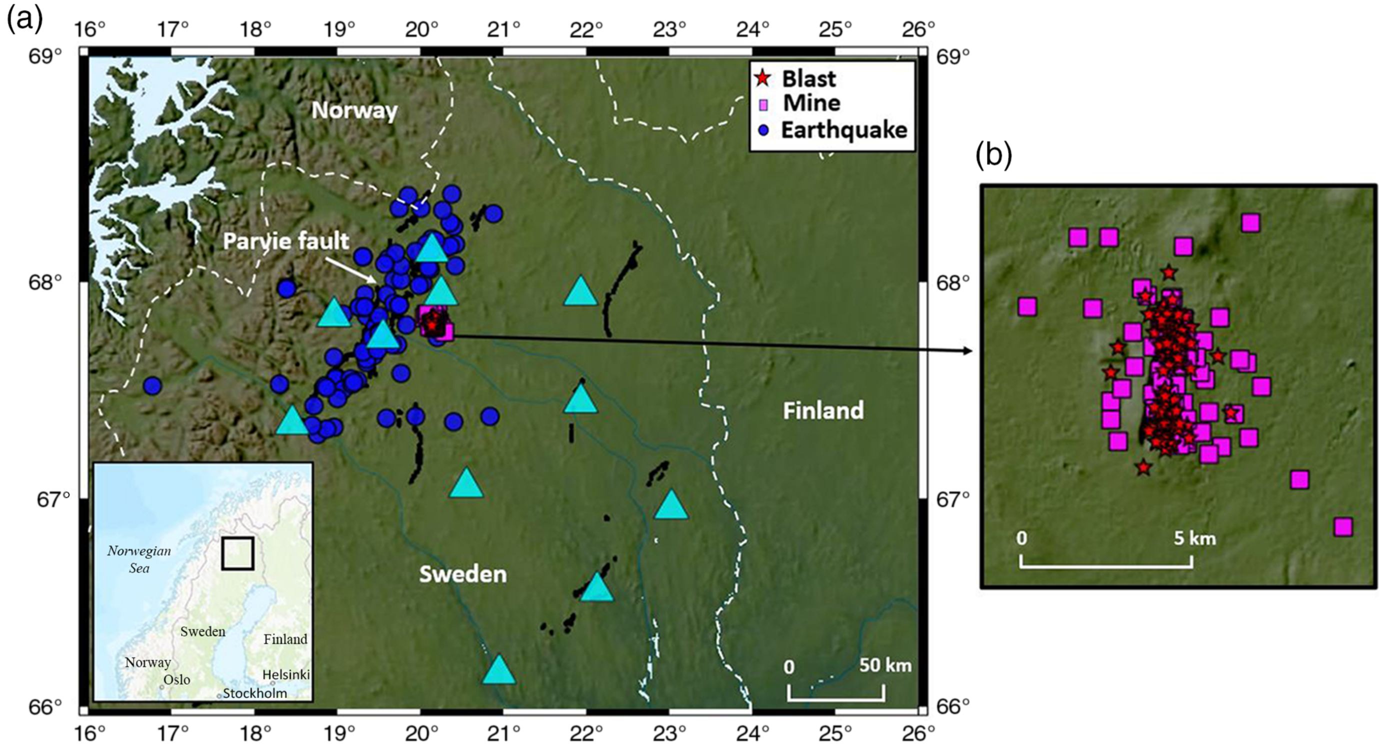

Figure 2. (a) The distribution of seismic stations and events in northern Sweden used in this study. The cyan triangles represent locations of surface seismic stations in the Swedish National Seismic Network (SNSN). The blue circles show earthquake locations within and adjacent to the Pärvie fault (solid black lines, also other postglacial faults). The study area is shown by the small box in the inset map. (b) Location of the Kiruna iron ore mine. The red stars and the magenta squares in the map show the location of blast and mining-related events, respectively. The color version of this figure is available only in the electronic edition.

In the Kiruna mine, blasting is done by drilling up to 10 boreholes in a fan shape. The longest central hole is about 50 m long, and the side holes are progressively shorter. Blasting is done with multiple charges per hole in sequence starting the farthest away in the central hole. About 20 individual charges in the fan are detonated. Some charges are detonated in sequence and others simultaneously. The charges are detonated in 25 ms intervals in a sequence that can be up to 200 ms long. Mine-related events are associated with tensile failure typically resulting from fracturing at excavation faces or from pillar collapses from highly stressed rock volumes (Dineva and Boskovic, 2017). Natural earthquakes are associated with slip along faults within the Pärvie fault system (Lindblom *et al.*, 2015; Lund *et al.*, 2021).

DATA AND METHODS

Seismic data

Kloof data. The 75 events used that occurred between March 2017 and November 2018 were recorded on five surface seismic networks (Fig. 1). These networks consist of 43 three-component accelerometers with sample rates of 200 samples/s, and two three-component broadband seismometers with sample rates of 100 samples/s. The broadband stations are part of the South African National Seismograph and AfricaArray networks, and the accelerometers are from the Western Deep seismic network (11 stations), the Strategic Water management project network (12 stations), and the Klerksdorp–Orkney–Stilfontein–Hartebeesfontein (KO) network (20 stations), which were deployed by the South African Council for Geoscience (CGS) to monitor seismicity related to mining activities and controlled flooding of worked-out mines in both operational and abandoned mines. All the seismic data used have been provided by the CGS.

The seismic event catalog used is from Masethe (2022) and Masethe *et al.* (2023), and contains three source types, crush (ISO), crush-slip (CLVD), and pure-slip (DC), identified using MTs calculated using in-mine seismic data. The in-mine seismic network is comprised of 4.5 Hz triaxial geophones recording at 6000 samples/s. For estimating MTs, Masethe *et al.* (2023) used data at stations located within a source radius of ∼1000 m, providing a hypocentral location uncertainty of <3%. Of the 75 MT solutions reported by Masethe *et al.* (2023), 50 are pure-slip (DC) events and have local magnitudes from 1.5 to 2.7 and focal depths from 1.6 to 4.2 km (Fig. 3a,d). Twenty-five of the 50 pure-slip events were located on known faults and dikes in the mine, and have MTs with a >60% DC component. Nineteen events are crush-slip (CLVD) events, and have local magnitudes of 1.5–2.5 and focal depths of 1.7–3.8 km (Fig. 3b,e). Six events are crush (ISO) events, and have local magnitudes of 1.5–2.7 and focal depths of 2.6–3.4 km

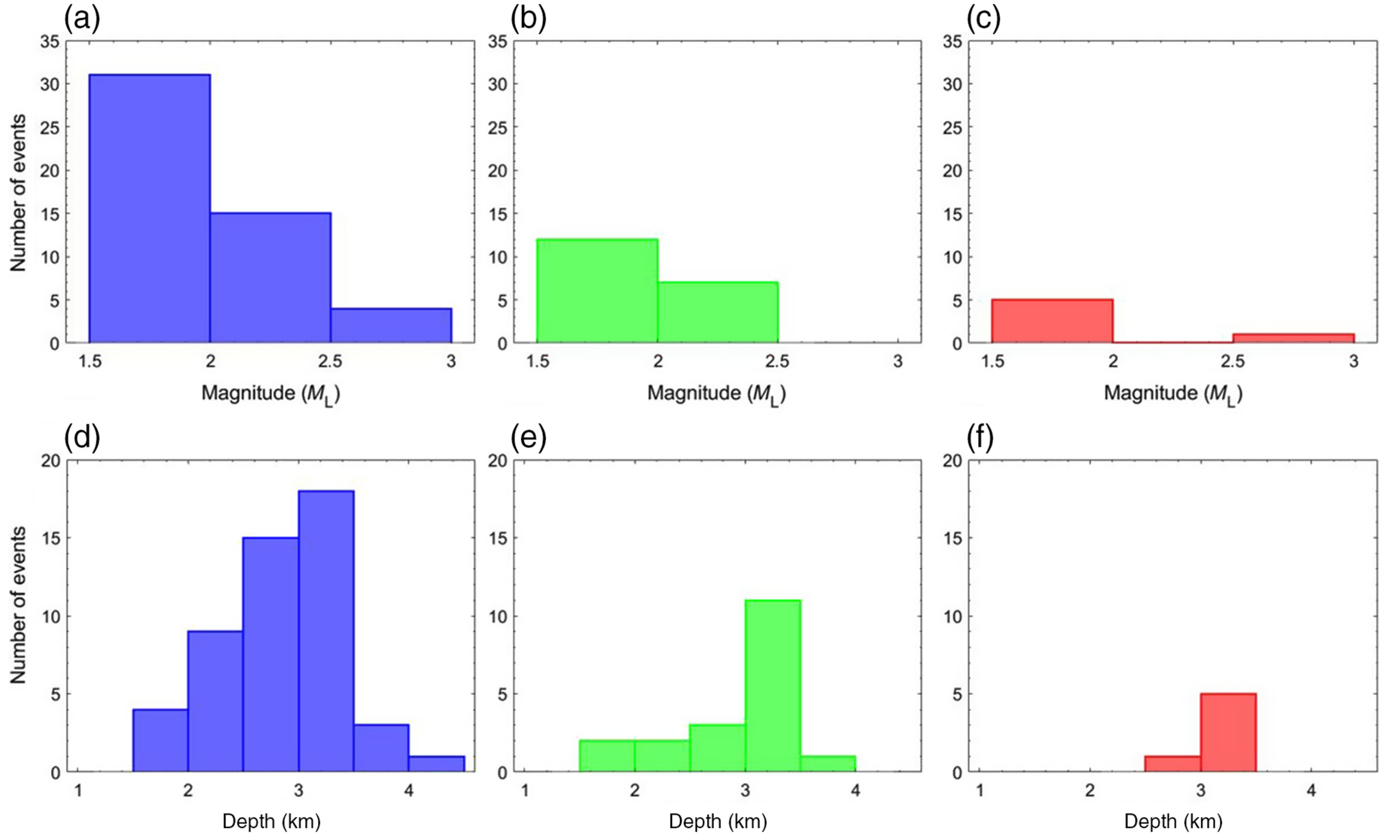

Figure 3. Histograms showing the number of events versus (a–c) local magnitude and (d–f) source depth for (a,d) pure-slip, (b,e) crush-slip, and (c,f) crush events in Kloof dataset. The color version of this figure is available only in the electronic edition.

(Fig. 3c,f). The magnitudes, focal depths, and source information for the seismic events are provided in Tables S1 and S2.

Kiruna data. We used data from 90 events from each source type (e.g., blast, mining-related, and earthquake) recorded by 11 surface stations within the Swedish National Seismic Network (SNSN, Lund *et al.*, 2021; SNSN, 2024; Fig. 2). The stations consist of three-component broadband seismometers with sample rates of 100 samples/s. The data used were provided by the SNSN data management center in Uppsala, Sweden.

Event information was taken from the SNSN catalog. The SNSN analysts determine the event type based on location, depth, time of day, and waveform characteristics. The explosions used in the study are taken from a list of blasts in the mine provided by the mining company. The ore body is 4 km long, and the blasts are located within the ore body. Mine-related events are located with the same accuracy as the blasts but have different waveform characteristics than the blasts (e.g., the *Rg* wave).

Earthquakes on the Pärvie fault located away from the mine. The earthquakes range from M_L 0.3 to 3.6 and are located at depths from ∼0.1 to 37 km along or close to the Pärvie fault system (Fig. 2). The blasts (chemical explosions) range from M_L 0.7 to 1.9 at depths ∼700–900 m, and the mining-related events range from M_L 0.7 to 2.1 at depths between 700 and 1000 m. The catalog information (magnitudes, depth, and source type) is given in Table S3 and summarized in Figure 4. The SNSN uses a moment-based local magnitude scale for earthquakes (Lund *et al.*, 2021), and a time domain Richter-type local-magnitude scale (Uski and Tuppurainen, 1996; Wahlström, 1979) for blast and mining-related events.

Data processing and measurements

Instrument responses were deconvolved from the raw seismograms prior to converting to displacement. The displacement seismograms for each event were cut to begin 10 s prior to the event origin time and 120 s after the event origin time for Kloof data, and 10 s prior to the event origin time and 90 s after the event origin time for the Kiruna data, ensuring body-wave phases were well recorded at all distance ranges. The 130 s long and 100 s long records were then rotated to vertical, radial, and transverse components (Z, R, and T), demeaned, detrended, and tapered, and filtered with four-pole two-pass Butterworth bandpass filters. Pass bands in 2 Hz intervals from 2 to 30 Hz were used. Example record sections for each event type for the Kloof and Kiruna data are shown in Figures S5–S10.

Amplitudes were measured using windows for *P* and S waves based on handpicked *P*- and *S*-wave arrivals. For the

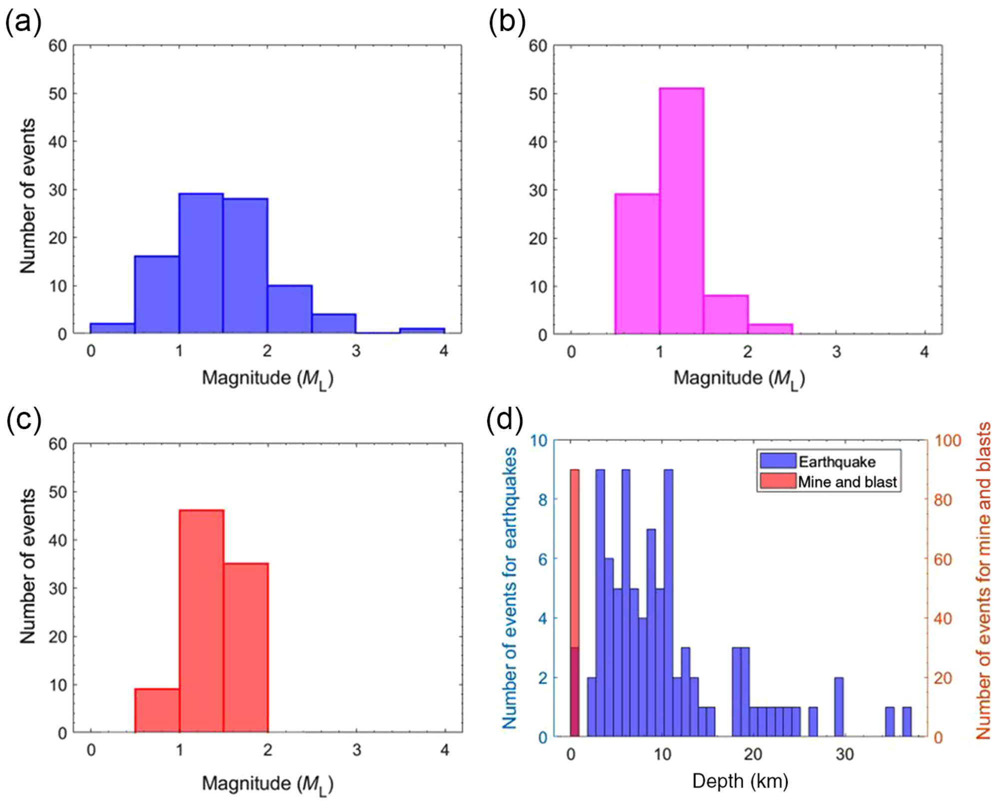

Figure 4. Histograms of number of events versus (a–c) local magnitude and (d) source depth for (a) earthquake (blue), (b) mine (magenta), and (c) blast (red) events in the Kiruna dataset. Because blast and mine events (90 events from each category) occur at depths of <1 km, in Figure 4d a single red column represents both blast and mine events. The color version of this figure is available only in the electronic edition.

Kloof data, the P window starts 0.1 s before the picked P arrival and ends 0.5, 1, and 2 s after the P arrival for distances <10 km, 10–20 km, and >20 km, respectively. The S window starts at 0.1 s before the picked S arrival and ends at 4 s later for all distances. For the Kiruna data, the P window starts 0.1 s before the picked P arrival and ends 1 and 2 s after the P arrival for distances <20 km and >20 km, respectively. The S window starts at 0.1 s before the S pick and ends at 5 s from the S pick for all distances.

An example of the time windows used for the Kloof data is shown in Figure 5. Each waveform was visually checked to ensure that the signal window lengths accurately captured the correct signal. This was done for each pass band to confirm that each seismic record used had a good signal-to-noise ratio for each pass band. Records in which it was difficult to visually pick P and S arrivals, and also events recorded on <3 stations, were excluded from further analysis.

P and S amplitudes were calculated by taking the rms of the vertical (Z), radial (R), and transverse (T) components within the P- and S-wave windows. The maximum rms value among Z, R, and T components was obtained for P and S wave for each seismic record. This approach ensures the inclusion of the full amplitude for each arrival, regardless of incident angles or polarization of the seismic wave, and yields similar results to the amplitude measurement methods used by others (e.g., O'Rourke *et al.*, 2016; Pyle and Walter, 2019). A correction was then applied to remove site amplification and distance propagation effects on each measurement before computing the amplitude ratios. The methodology followed for this correction is described in Kintner *et al.* (2020) and briefly summarized subsequently.

Regression analysis

The observations (e.g., measured amplitudes) were used to construct an average propagation model, which aims to reduce the station amplification due to the variation in underlying site geology, and the amplitude–distance dependence resulting from attenuation and/or geometric spreading. The observations were fit using a linear regression model that decomposes the P- and S-wave amplitude measurements into convolutions of source, site amplification, and geometrical spreading and attenuation terms (Malagnini *et al.*, 2000). The governing equation, which satisfies the logarithm of the convolutional factors in the frequency domain, is as follows:

$$\log_{10}(A_m) = \log_{10} \mathrm{EXC}(f')_i + \log_{10} \mathrm{SITE}(f')_j + \log_{10} G(r_j, f'), \quad (1)$$

in which A_m indicates mth P- or S-wave amplitude observation; EXC indicates source excitation term for source i; SITE indicates site amplification term for station j; G indicates distance term; and r_j indicates observed source–station distance. The terms in equation (1) are a function of frequency, but the observed amplitudes were measured across specific bandwidths (i.e., 2–4 Hz, 4–6 Hz etc.). Therefore, equation (1) represents an average value across the measurement bandwidths. This approach is similar to the magnitude–distance correction approach of Walter and Taylor (2001) but differs in that it fits the observed amplitude decay with distance resulting from geometrical spreading and attenuation, which may change rapidly at local distances (Kintner *et al.*, 2020).

P- and S-wave amplitudes were inverted for separately using equation (1) for each frequency range by linearizing the

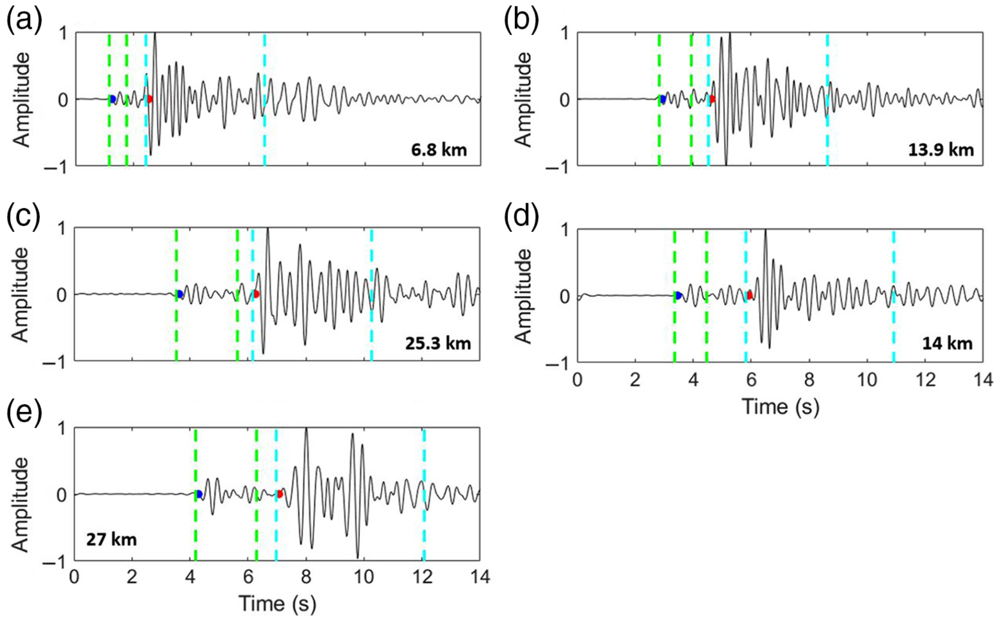

Figure 5. Illustration of the time windows used to obtain amplitude measurements for *P* and *S* waves for an event recorded at (a) 6.8 km, (b) 13.9 km, and (c) 25.3 km from the Kloof mine, events recorded at (d) 14 km and (e) 27 km from the Kiruna mine. The blue and red dots represent manually picked *P*- and *S*-wave onset times, and the green and cyan dashed lines represent corresponding signal windows. The *Y*-axis represents normalized amplitudes. The waveforms are filtered from 2 to 4 Hz. The color version of this figure is available only in the electronic edition.

distance factor (G), as described in Kintner *et al.* (2020). The distance factor was parameterized using a piecewise linear function defined at a series of nodes over a range of source–receiver distances (0.001, 5, 10, 15, 25, 50, 75, 100, and 130 km for the Kloof dataset and 0.001, 5, 10, 25, 75, 100, 150, 200, and 260 km for the Kiruna dataset), and solved for a combined geometrical spreading and attenuation factor at each node. The distance correction term was calculated for each measurement by linearly interpolating the distance factor between nearby nodes. The number of nodes and the spacing of the nodes were defined based on the observed source–receiver distances. The linearized equation for one observation (observed source-station distance: r_j) between the distance r_k and r_{k+1} has the following form:

$$\log_{10}(A_m) = \log_{10} \mathrm{EXC}(f')_i + \log_{10} \mathrm{SITE}(f')_j + q \log_{10} G(r_k, f') + p \log_{10} G(r_{k+1}, f'), \quad (2)$$

in which $q = 1 - p$, distance-dependent constant $(p) = \frac{r_j - r_k}{r_{(k+1)} - r_k}$; r_j indicates observed source–station distance; and r_k and r_{k+1} indicate node distances corresponding to lower and higher than observed source–receiver distance, respectively. Equation (2) was used in the regression analysis for estimating source, site, and distance correction factors, including geometrical spreading and attenuation for each observation.

To stabilize the regression, several constraints were applied for the site and distance terms. The logarithm of the site terms was summed for all stations to zero, which eliminates any bias in the site terms (Kintner *et al.*, 2020). For the distance term, an initial model was used that follows a simple geometrical spreading function of $1/r$ for both *P*- and *S*-wave inversion, and then a weight constraint was added for all nodes to get the ideal geometrical spreading values (see example in Figs. S11 and S12). The constraints may shift the absolute amplitude of the source term but does not affect the source term ratios (Kintner *et al.*, 2020).

All the regressions were computed using the singular value decomposition method, and equation (3) was used to estimate the corrected amplitude (A_c) for *P* and *S* waves,

$$\log_{10}(A_c) = \log_{10}(A_o) - \log_{10}(A_{\mathrm{SITE}}) - \log_{10}(A_G) = \log_{10}(A_{\mathrm{EXC}}), \quad (3)$$

in which A_o indicates observed amplitude; A_{SITE} indicates model predicted amplitude as a result of site amplification; A_G indicates model predicted amplitude due to geometrical spreading and attenuation; and A_{EXC} indicates model predicted amplitude from the source effect. The corrected amplitudes were then used to compute the *P/S* ratios.

In the regressions, to obtain the source excitation terms, all the nodes were fixed in the attenuation function, and the all-site terms were set to sum to zero. As a result, the value of all source excitation factors may include a constant component of the propagation or site effects, and that constant may differ for *P* and *S*.

We followed the Aster *et al.* (2013) methodology to estimate uncertainties of each term in equation (1). The least-squares uncertainties of each model parameter in the equation are computed by scaling the normalized model covariance matrix by the data variance. The data variance is estimated from the residual of the least-squares solutions. The formal variance estimates for the model parameters may vary due to the location of the event as well as due to the number of observations (Kintner *et al.*, 2020).

Figures 6 and 7 show *P* and *S* source excitation terms plotted versus each event magnitude with uncertainties (error bars)

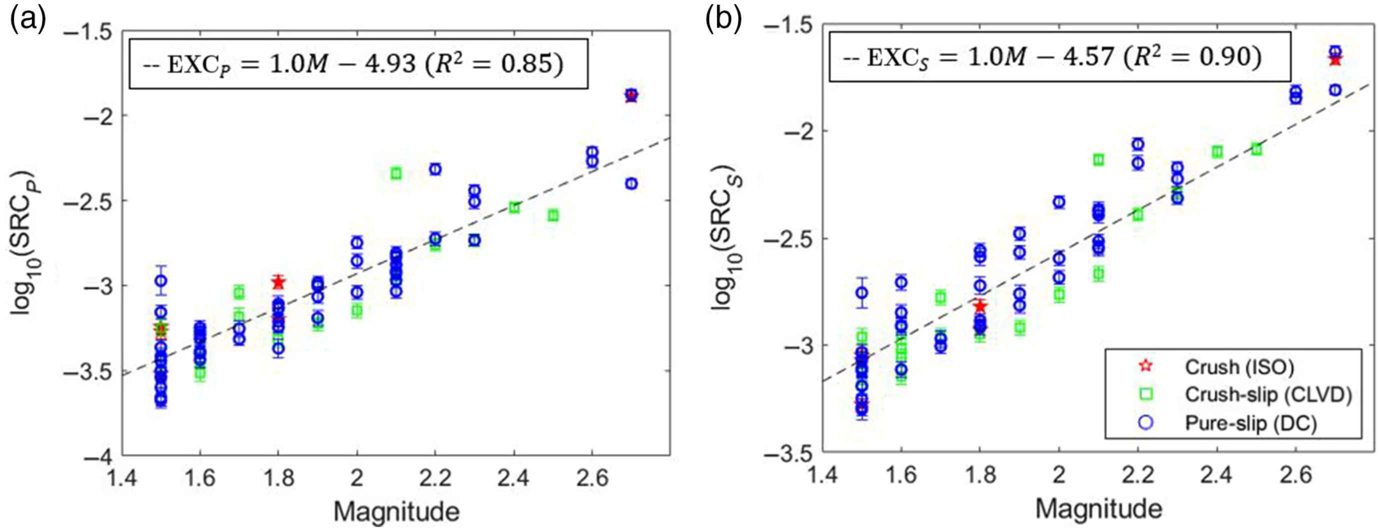

Figure 6. (a) *P* and (b) *S* source excitation terms (SRC) plotted as a function of local magnitude from linear regression analysis at 2–4 Hz for the Kloof dataset. The dashed lines are fits to the local magnitude estimates with a slope of 1.0. The R^2 values are for the regression lines shown. The red stars represent crush (ISO) events, green squares represent crush-slip (compensated linear vector dipole [CLVD]) events, and blue circles represent pure-slip (double-couple [DC]) events. The color version of this figure is available only in the electronic edition.

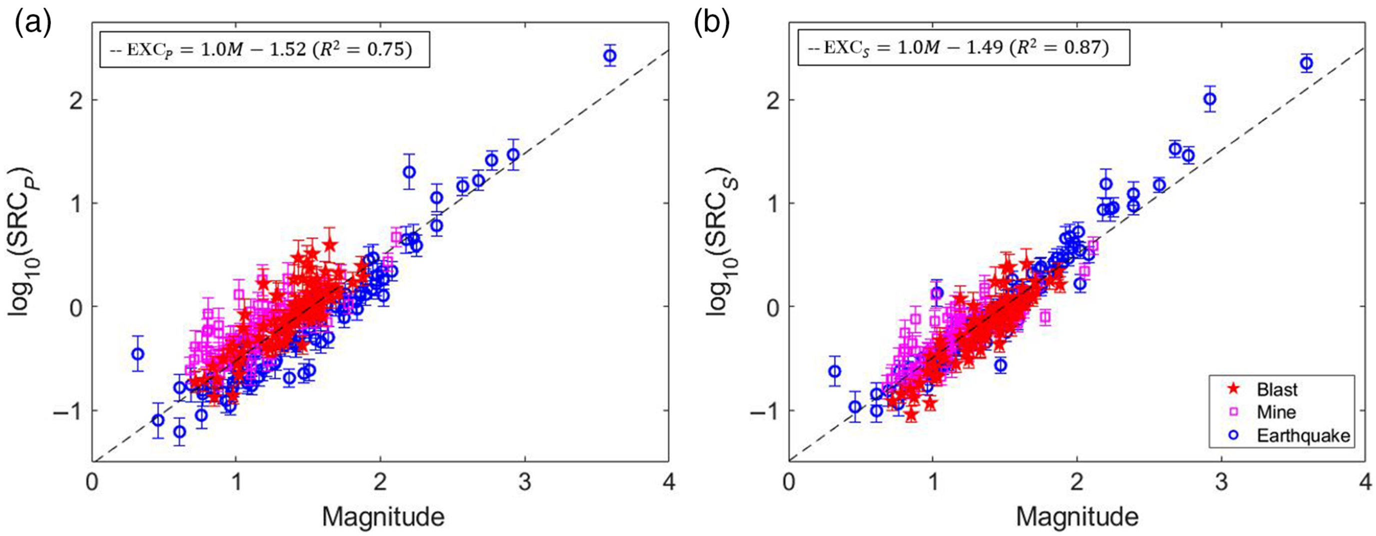

Figure 7. (a) *P* and (b) *S* SRC plotted as a function of local magnitude from linear regression analysis at 4–6 Hz for the Kiruna data. The dashed lines are fits to the local magnitude estimates with a slope of 1.0. The R^2 values are for the regression lines shown. The stars represent blasts, squares represent mine-related events, and circles represent earthquakes. The color version of this figure is available only in the electronic edition.

for selected pass bands (2–4 Hz for Kloof data and 4–6 Hz for Kiruna data), illustrating that the size of the source terms correlates well with event magnitude. A line with a unit slope fits both *P* and *S* measurements fairly well, despite some scatter in the data points, as expected from the direct proportionality between event amplitude and magnitude. That plots for both the datasets follow the expected first-order linear pattern provides confidence in adequate separation between the source and propagation effects by the regression analysis.

RESULTS

Kloof data

Figure 8a shows average *P*/*S* amplitude ratios in 2 Hz pass bands from 2 to 30 Hz for the 75 Kloof events classified by MT solutions. It should be noted that an uneven number of events for each source type is used in our amplitude ratio comparison. Based on the estimated ratios, events with a DC component ≥60%, which also have been located on known faults and dikes (Masethe *et al.*, 2023; Table S2), separate from the

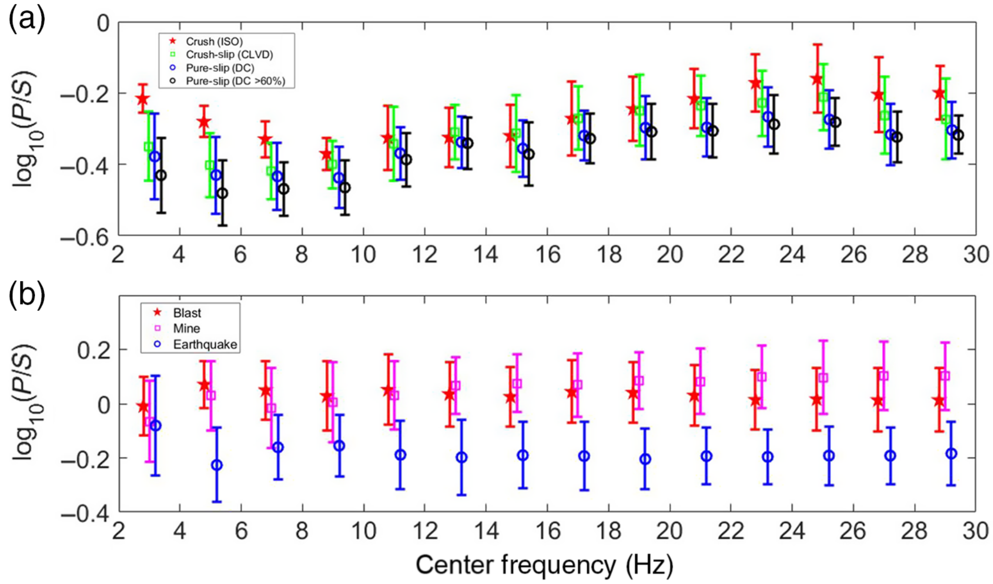

Figure 8. (a) Average $\log_{10}(P/S)$ values calculated using waveforms filtered at a range of frequency bands for the Kloof dataset, plotted at the center frequency of each band and with one standard deviation error bars. The red stars indicate crush (isotropic) events; green squares indicate crush-slip (CLVD) events; blue circles indicate all pure-slip (DC) events; and black circles indicate confirmed pure-slip (>60% DC) events. (b) Average $\log_{10}(P/S)$ values for the Kiruna dataset calculated using waveforms filtered at a range of frequency bands plotted at the center frequency of each band and with one standard deviation error bars. The stars indicate blast; squares indicate mine related; and circles indicate earthquake sources. The color version of this figure is available only in the electronic edition.

isotropic (crush, ISO) events in the 2–8 Hz frequency pass band without any overlap in the one standard deviation error bars. Isotropic (i.e., crush, ISO) events separate from the all DC (pure-slip) events in the 2–6 Hz frequency pass bands, but the one standard deviation error bars slightly overlap by 1%–2%. The crush-slip (CLVD) events also separate from crush (ISO) events in the 2–6 Hz frequency pass bands, but there is a small but likely nonsignificant (<10%) overlap in the one standard deviation error bars. In comparison, the crush-slip (CLVD) events cannot be distinguished from the DC events for any frequency range. For higher pass bands (i.e., >8 Hz), there is significant overlap in the one standard deviation error bars for all source types (i.e., ISO, CLVD, and DC events). To ensure that there are no additional azimuthal or distance effects contributing to the overlap in the error bars at pass bands of >8 Hz, we examined separately the network-averaged *P*/*S* ratios of each event, because stations in each network lie within different azimuthal ranges (Fig. S13), and then the average amplitude ratios of station–event pairs within distance ranges 0–50 km, 50–100 km, and 100–130 km (Fig. S14). In those figures, even though slight differences in average amplitude ratios can be seen, there is significant overlap in the one standard deviation error bars for all frequency bands, and therefore no azimuthal and distance effects on the amplitude ratios can be discerned. These results thus indicate that amplitude ratios can separate (i.e., discriminate) isotropic (crush type) from DC (pure-slip) mining sources for the lowest frequencies. Similar results are obtained if 4 Hz pass bands are used (Fig. S15).

To examine if *P* and *S* source excitation terms can also be used as a discriminant, results in the 2–4 Hz pass band are examined, because results in that pass band show the most separation between the average *P/S* amplitude ratios (Fig. 8a). The *P*- and *S*-wave source excitation factors for each event type show strong correlation (Fig. 9a) and little to no separation. Thus, no clear pattern exists in the source terms that can be used for source discrimination.

Kiruna data

Figure 8b illustrates average *P/S* amplitude ratios in 2 Hz pass bands from 2 to 30 Hz for the Kiruna data. Blast events are best separated from earthquakes between 4–6 Hz and 18–22 Hz without any overlap of the one standard deviation error bars. In addition, in the 10–18 Hz and 22–28 Hz bands, the one standard deviation error bars overlap by only ~1%–10%. Mining-related events are best separated from earthquakes at frequencies ≥10 Hz, with the minimal overlap (<12%) in the one standard deviation error bars in the 10–12 Hz pass band. There is a significant overlap in the one standard deviation error bars for blast and mining-related events for all frequencies. To ensure there are no additional azimuthal or distance effects contributing to the overlap in the error bars at all pass bands, we examined separately the average *P/S* ratios of station–event pairs within distance ranges of 0–50 km, 50–100 km, and 150–200 km (see Fig. S16) and average amplitude ratios within three different azimuthal ranges (see Fig. S17). In those figures, even though slight differences in average amplitude ratios can be seen, there is significant overlap in the one standard deviation error bars for all frequency bands, and therefore no azimuthal and distance effects on the amplitude ratios can be discerned. Like the Kloof dataset, the results for the Kiruna dataset indicate that amplitude ratios can separate (i.e., discriminate) earthquakes (DC) from blasts (ISO; 4–6 Hz and 10–28 Hz) and earthquakes from mining-related events (>10–12 Hz) for certain frequency bands. Similar results are obtained if 4 Hz pass bands are used (Fig. S15).

To check if the *P* and *S* source excitation terms can be used as a discriminant, we use results in the 4–6 Hz pass band, the

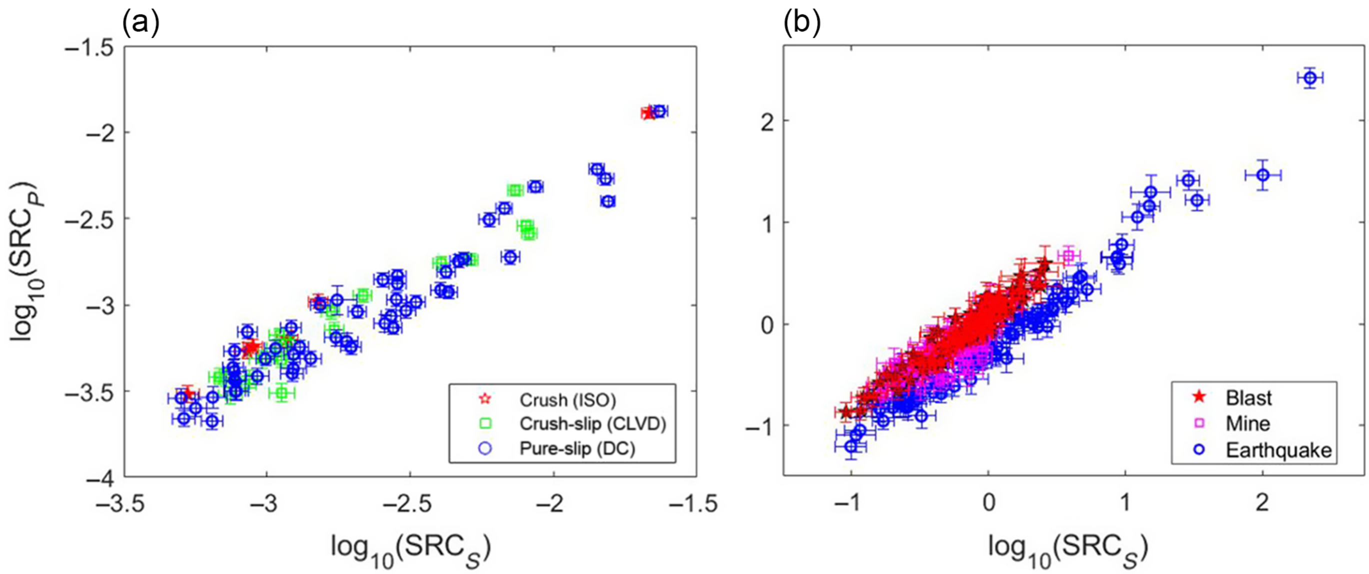

Figure 9. (a) SRCs from the linear regression analysis of *P* and *S* amplitude measurements at 2–4 Hz for the Kloof dataset. The red stars represent crush (ISO) events, green squares represent crush-slip (CLVD) events, and blue circles represent all pure-slip (DC) events. (b) SRCs from the linear regression analysis of *P* and *S* amplitude measurements at 4–6 Hz for the Kiruna dataset. The stars indicate blast; squares indicate mine-related; and circles indicate earthquake sources. The color version of this figure is available only in the electronic edition.

best frequency range for all the sources showing minimal overlap of the one standard deviation error bars (Fig. 8b). Figure 9b shows *P* source excitation terms for each event plotted versus their *S* source excitation factors, and the *P* and *S* source excitations terms from earthquakes, mine blast, and mine sources show little separation, and thus cannot be used for source discrimination like the Kloof dataset.

DISCUSSION

To summarize, *P/S* amplitude ratios obtained for some frequency bands using data from local (<130 km for Kloof and <260 km for Kiruna) surface seismic stations discriminate between isotropic and DC mine-related events in the Kloof Gold mine, and between chemical explosions (blasts) in the Kiruna mine and earthquakes along the Pärvie fault system. For the Kloof dataset, *P/S* amplitude ratios for crush (isotropic sources) and pure-slip (all DC sources) events are well separated from 2 to 6 Hz, and from 2 to 8 Hz (Fig. 8a) for events with a dominant DC (i.e., DC component ≥60%). This result can be attributed to the larger lower frequency shear waves generated by DC events compared to isotropic events. The *P/S* amplitude ratio does not discriminate between the crush-slip (CLVD) and pure-slip (DC) events (Fig. 8a). In addition, source excitation terms do not discriminate between source types (Fig. 9a).

For the Kiruna dataset, *P/S* amplitude ratios for chemical explosions and earthquakes separate within pass bands of 4–6 Hz and 18–22 Hz (Fig. 8b). In addition, the one standard deviation bounds of the *P/S* amplitude ratios have minimal overlap (<10%) for the 10–18 Hz and 22–28 Hz pass bands, which further suggests an overall plausible separation between 4–6 Hz and 10–28 Hz. In addition, separation of *P/S* amplitude ratios shows that mine-related events can be discriminated from earthquakes at frequencies of ≥10 Hz. This is in agreement with a recent seismic event discrimination study in Sweden using fully connected neural networks (Eggertsson *et al.*, 2024), which found that features in 3 Hz pass bands between 12 and 41 Hz are of high importance for the separation of event types. At the lowest frequencies, there is significant overlap in the one standard deviation uncertainties between earthquakes and the other source types (i.e., 2–4 Hz and 6–10 Hz with blasts and 2–10 Hz with mine events). Similar to the Kloof mine results, source excitation terms do not discriminate between source types (Fig. 9b).

We also find poor discrimination performance between blasts and mine-related events at any frequency. Even though mine-related events may contain crush, crush-slip, and pure-slip-type events, similar to Kloof dataset, the dataset used in this study contains mostly crush-type (e.g., mine collapse) sources (personal communication, seismic network operators Kiruna mine and SNSN), which may explain the lack of amplitude ratio separation between blasts and mine events. To investigate this possibility, we performed grid search full MT inversions for 25 selected mine events using the methodology summarized in Herrmann *et al.* (2008). The MT solutions for all the events have a dominant isotropic component (Table S4). An example solution (see event id-234 in Table S3) is shown in Figures S18 and S19. A dominate isotropic component in the MT solutions supports the inference that the mine sources in the Kiruna dataset are mainly crush type (isotropic).

Our finding that *P/S* amplitude ratios in the 2–8 Hz frequency range for mine-related events in the Kloof dataset and 4–6 Hz for the Kiruna dataset can discriminate between isotropic and pure-slip events is similar to findings reported by other studies for larger events (**M** > 4) recorded at regional and teleseismic distances, as mentioned in the Introduction section. A number of *P/S* discriminant studies for events recorded at regional and teleseismic distances (e.g., Walter *et al.*, 1995, 2018; Taylor, 1996; Taylor *et al.*, 2002) have identified low-frequency (<10 Hz) separation of explosion sources (i.e., isotropic) from earthquakes (i.e., pure-slip). For example, Walter *et al.* (1995) noted *P/S* ratios of earthquakes, and explosions from Nevada test site (NTS) show separation when ratios are averaged in the 6–8 Hz pass band, while Taylor (1996), from an analysis of 294 explosions at NTS and 114 earthquakes from the western United States, found that mean *P/S* ratios can discriminate sources in the 2–10 Hz pass band. The effective 2–8 Hz (Kloof) and 4–6 Hz (Kiruna) pass bands at the lower end of the frequencies analyzed in this study for locally recorded small events is similar to results for larger events recorded at greater distances.

Our findings for the Kiruna dataset are also consistent with other local-distance (<300 km) *P/S* discriminant studies (e.g., Kim *et al.*, 1997; O'Rourke *et al.*, 2016; Pyle and Walter, 2019), which show that chemical explosions and earthquakes can be discriminated using frequency pass bands between 6 and 22 Hz. However, we only see a clear separation of amplitude ratios up to 8 Hz for the Kloof dataset. The differences in the frequency band for the Kloof dataset (≤8 Hz) compared with the Kiruna dataset and the other above referenced studies (>8 Hz) could arise from one or more of the following: (1) crustal attenuation (intrinsic and scattering) of high-frequency shear waves (Eulenfeld and Wegler, 2017); (2) near-source and near-receiver high-frequency body-wave scattering (Ebel, 1989; Hardebeck and Shearer, 2003); (3) focusing and defocusing effects caused by small-scale velocity heterogeneity resulting in large amplitude differences among even closely spaced events (Hardebeck and Shearer, 2003); (4) event radiation patterns causing significant amplitude differences at different receivers; (5) influence of larger stopes (i.e., larger excavations or voids that may extend for many kilometers) and pillars on seismic wave propagation (Linzer *et al.*, 2019, 2021); and (6) greater attenuation of body waves due to damage of surrounding underground rock from old mining activities (Wesseloo *et al.*, 2009). Of the possible influences listed, the large stopes and pillars (Linzer *et al.*, 2019, 2021) in the Kloof mine may uniquely influence wave propagation at local distances and thus could plausibly be the reason why our results for the Kloof dataset do not show separation in the *P/S* amplitude ratios above 8 Hz.

The potential influence of source depth on the *P/S* amplitude discriminant has been discussed for both regional/teleseismic and local studies (e.g., Walter *et al.*, 1995, 2018; Taylor, 1996; Taylor *et al.*, 2002; O'Rourke *et al.*, 2016; Pyle and Walter, 2019), and can be addressed directly with the Kloof dataset because source depths are accurately constrained using in-mine network data. The crush-type events (ISO) all occur within a 1 km depth range below the surface (2600–3600 m depths), as do many of the pure-slip events which have a dominant DC component (i.e., DC >60%; Fig. 3). Thus, any depth effect on the discriminant can be directly evaluated. Figure 10a shows results for these event types within the 2600–3600 m depth interval. The average amplitude ratio of the dominant pure-slip events shows clear source separation with the crush-type events. These results clearly illustrate that the amplitude ratio is not influenced by source depth, at least not for the Kloof mine.

The influence of source depth on *P/S* amplitude ratios can also be examined using the earthquakes in the Kiruna dataset. Figure 10b shows results for the average ratios calculated for shallow (<10 km depth; number of events (N) = 53) and deep focus (>20 km; $N = 11$) earthquakes for the 4–6 Hz pass band. The result shows that amplitude ratios for earthquakes do not show any notable depth effect, which further indicates that the ratios are not sensitive to source depth.

SUMMARY AND CONCLUSIONS

We have used crush (ISO), crush-slip (CLVD), and pure-slip (DC) events from the Kloof gold mine in South Africa, classified by MT solutions, and earthquakes, chemical blast, and mine-related events from within and near the Kiruna iron ore mine in northern Sweden, to investigate if *P/S* amplitude ratios for small events recorded the local distances of <130 km (Kloof mine) and <260 km (Kiruna mine) can discriminate between source types. Our results for the Kloof mine show that *P/S* amplitudes, estimated in the 2–6 Hz frequency band, discriminate between isotropic (i.e., crush type) and DC (pure slip) events. If only pure-slip events with a DC component >60% are considered, then the effective frequency band can be extended from 2 to 8 Hz. These frequency bands (2–6 and 2–8 Hz) are similar to the effective frequency bands reported by other studies evaluating the efficacy of the *P/S* amplitude discriminant using larger events recorded at regional and teleseismic distances.

Our results for the Kiruna mining region show that *P/S* amplitude ratios discriminate earthquakes from underground chemical mine blasts for pass bands of 4–6 Hz and 18–22 Hz. In addition, the one standard deviation error bars for the average *P/S* amplitude ratios have minimal overlap (<10%) for the 10–18 Hz and 22–28 Hz pass bands, which further suggests an overall plausible separation between 4–6 Hz and 10–28 Hz. These results are generally consistent with the previously reported results for small locally recorded seismic events. For example, Pyle and Walter (2019) noted that earthquakes and chemical explosions can be discriminated above 6 Hz, with some plausible separation above ∼4 Hz when average amplitude ratios are computed at various distance ranges (e.g., distances <50 km). Similarly, O'Rourke *et al.* (2016) reported that *P/S* amplitude ratios effectively separate mine blasts from

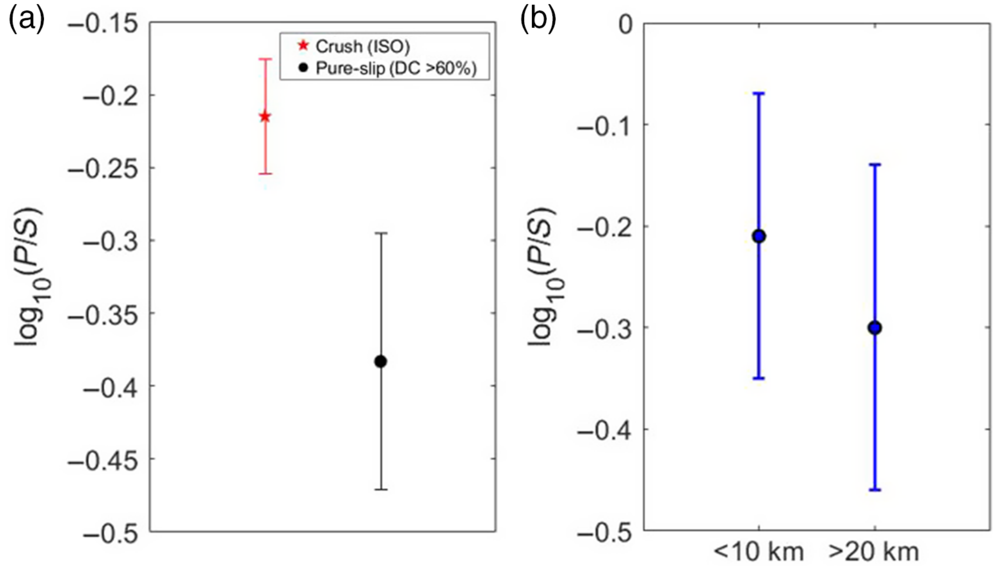

Figure 10. (a) Source-type average amplitude ratios in the 2–4 Hz pass band calculated for the crush (six events) and dominant pure-slip (16 events) events with source depths between ∼2.6 and 3.6 km in the Kloof mine. Error bars show ±1 standard deviation. The red star indicates crush (ISO) events; and black circle indicates dominant pure-slip (≥60% DC) events. (b) Average amplitude ratios for earthquakes in the Kiruna dataset at shallower (<10 km) and deeper (>20 km) depths for the 4–6 Hz pass band. Error bars show ±1 standard deviation. The color version of this figure is available only in the electronic edition.

earthquakes in the 6–10 Hz pass band and show plausible separation up to 16 Hz with only small overlaps (<10%–20%) in the error bars. Our results further suggest successful discrimination between mine-related events and earthquakes at frequencies of 10–12 Hz and higher for the Kiruna dataset. Thus, overall, our findings for both the Kloof and Kiruna datasets suggest that the *P/S* amplitude ratio discriminant can be extended to small events recorded at local distances.

Because source depths in the Kloof mine are accurately constrained using in-mine network data, potential depth effects on *P/S* amplitude ratios were evaluated. A comparison of amplitude ratios for crush (isotropic) and pure-slip (DC) events located within a 1 km depth range shows that the amplitude ratios are not influenced significantly by source depth. Similarly, a lack of depth dependence of average amplitude ratios for earthquakes in the Kiruna dataset further suggests that source depth does not significantly influence *P/S* amplitude ratios.

DATA AND RESOURCES

Seismic waveforms for the Kloof mine events were obtained from the Council for Geosciences (CGS) in South Africa. Seismic data (events and waveforms) for Kiruna region were obtained from the data management center of the Swedish National Seismic Network (SNSN) in Uppsala, Sweden, doi: 10.18159/KIR-EBI23. The catalog of blasts, mine-related events, and earthquakes were obtained from the SNSN. Maps were generated using Generic Mapping Tool (GMT; Wessel *et al.*, 2019). The supplemental material contains tables and figures referenced in the main article, including event catalogs for the Kloof and Kiruna events, moment tensor (MT) solutions for the Kloof events, estimated MT solutions for selected mine events in the Kiruna mine, simplified geologic maps for Kloof and Kiruna regions, generalized stratigraphic column of Witwatersrand basin and Kiruna area, example record sections of Kloof and Kiruna events, solution to the distance terms (G) from the linear regression analysis for the Kloof and Kiruna data, network average/azimuth limited amplitude ratio plot for Kloof and Kiruna data set, average amplitude ratio at limited distance for Kloof and Kiruna data set, average $\log_{10}(P/S)$ amplitude ratio plots for the Kloof and Kiruna datasets, and an example of MT estimate for an implosive-type (mine collapse) mine event in the Kiruna mine and Rayleigh waveform comparison for the MT solution with the best-fit source depth.

DECLARATION OF COMPETING INTERESTS

The authors acknowledge that there are no conflicts of interest recorded.

ACKNOWLEDGMENTS

This research was supported by the Defense Threat Reduction Agency (Grant Number HDTRA1-17-1-0010) and Air Force Research Laboratory Space Vehicle Directorate (Grant Number RFI-541715). The facilities of the Swedish National Seismic Network (SNSN) data management center and Council for Geosciences (CGS) in South Africa were used for accessing the seismic waveform data used in this study. The authors thank Mirjana Boskovic, LKAB, for help identifying the Kiruna mine blasts. The authors thank Associate Editor Junghyun Park and two anonymous reviewers for helpful comments that improved this article.

REFERENCES

Aster, R. C., B. Brochers, and C. H. Thurber (2013). *Parameter Estimation and Inverse Problems*, Second Ed., Academic Press, Waltham, Massachusetts, p. 360.

Bayanova, T. B., J. Ludden, and F. P. Mitrofanov (2009). Timing and duration of Palaeoproterozoic events producing ore-bearing layered intrusions of the Baltic Shield: metallogenic, petrological and geodynamic implications, in *Palaeoproterozoic Supercontinents and Global Evolution*, S. M. Reddy, R. Mazumder, D. A. D. Evans, and A. S. Collins (Editors), The Geological society of London, London, United Kingdom, Special Publications, Vol. 323, 165–198.

Beach, A., and R. Smith (2007). *Structural Geometry and Development of the Witwatersrand Basin, South Africa*, Vol. 272, Geological Society, London, Special Publications, 533–542.

Boatwright, J., and J. B. Fletcher (1984). The partition of radiated energy between P and S waves, *Bull. Seismol. Soc. Am.* **74,** no. 2, 361–376.

Cliff, R. A., D. Rickard, and K. Blake (1990). Isotope systematics of the Kiruna magnetite ores, Sweden: Part I. Age of the ore, *Econ. Geol.* **85,** 1770–1776.

Coward, M. P., R. M. Spencer, and C. E. Spencer (1995). *Development of the Witwatersrand Basin, South Africa*, Vol. 95, Geological Society, London, Special Publications, 243–269.

Dankert, B. T., and K. A. Hein (2010). Evaluating the structural character and tectonic history of the Witwatersrand Basin, *Precambrian Res.* **177,** nos. 1/2, 1–22.

Dineva, S., and M. Boskovic (2017). Evolution of seismicity at Kiruna Mine, in J. Wesseloo (Editor), *8th Int. Conf. on Deep and High Stress Mining*, Perth, Australian Centre for Geomechanics, 125–140.

Diop, S., L. Heath, M. Malepe, P. Motjale, N. Mpanza, B. Msane, M. Radzilani, J. Rikhotso, M. Sebesho, B. Skhosana, *et al.* (2016). Geotechnical assessment of the KOSH area for seismic microzonation, *Rept. Number 2016-0079*, Council for Geoscience.

Ebel, J. (1989). The effect of crustal scattering on observed high-frequency earthquake seismograms, *Geophys. J. Roy. Astron. Soc.* **98,** 329–341.

Eggertsson, G., B. Lund, P. Schmidt, and M. Roth (2024). Earthquake or blast? Classification of local-distance seismic events in Sweden using fully-connected neural networks, *Geophys. J. Int.* doi: 10.1093/gji/ggae018.

Ernst, R., and W. Bleeker (2010). Large igneous provinces (LIPs), giant dyke swarms, and mantle plumes, significance for breakup events within Canada and adjacent regions from 2.5Ga to the Present, *Can. J. Earth Sci.* **47,** no. 5, 695–739.

Eulenfeld, T., and U. Wegler (2017). Crustal intrinsic and scattering attenuation of high frequency shear waves in the contiguous United States, *J. Geophys. Res.* **122,** 4676–4690, doi:10.1002/2017JB014038.

Gibowicz, S. J., and A. Kijko (1994). *An Introduction to Mining Seismology*, First Ed., Academic Press, Inc., San Diego, California.

Hardebeck, J. L., and P. M. Shearer (2003). Using S/P amplitude ratios to constrain the focal mechanisms of small earthquakes, *Bull. Seismol. Soc. Am.* **93,** no. 6, 2434–2444.

Herrmann, R. B., M. Withers, and H. Benz (2008). The April 18, 2008, Illinois earthquake—An ANSS monitoring success, *Seismol. Res. Lett.* **79,** 830–843.

Huber, M., (2023). Sustainable development opportunities for the Kiruna area (N Sweden), *Aspects Min Miner Sci.* **10,** no. 4, 000741, doi: 10.31031/AMMS.2023.10.000741.

Hudyma, M., and Y. H. Potvin (2010). An engineering approach to seismic risk management in Hardrock Mines, *Rock Mech. Rock Eng.* **43,** no. 6, 891–906.

Hunter, D. R., M. R. Johnson, C. R. Anhaeusser, and R. J. Thomas (2006). Introduction, in *The Geology of South Africa*, M. R. Johnson, C. R. Anhaeusser, and R. J. Thomas (Editors), Geological Society of South Africa/Council for Geoscience, South Africa, Pretoria, 1–7.

Jones, M. Q. W. (2003). Thermal properties of stratified rocks from Witwatersrand gold mining areas, *J. South. Afr. Inst. Min. Metall.* **103,** 173–186.

Julià, J., A. Nyblade, R. Durrheim, L. Linzer, R. Gök, P. Dirks, and W. Walter (2009). Source mechanisms of mine-related seismicity, Savuka mine, South Africa, *Bull. Seismol. Soc. Am.* **99,** no. 5, 2801–2814.

Keneti, A., and B. Sainsbury (2018). Review of published rock burst events and their contributing factors, *Eng. Geol.* **246,** 361–373.

Kim, W. Y., V. Aharonian, A. L. Lerner-Lam, and P. G. Richards (1997). Discrimination of earthquakes and explosions in southern Russia using regional high-frequency three-component data from the IRIS/JSP Caucasus Network, *Bull. Seismol. Soc. Am.* **87,** 569–588.

Kim, W. Y., D. W. Simpson, and P. G. Richards (1993). Discrimination of regional earthquakes and explosions in eastern United States using high-frequency data, *Geophys. Res. Lett.* **20,** 1507–1510.

Kintner, A. J., K. M. Cleveland, C. J. Ammon, and A. Nyblade (2020). Testing a local-distance Rg/Sg discriminant using observations from the Bighorn region, Wyoming, *Bull. Seismol. Soc. Am.* **110,** no. 2, 727–741, doi: 10.1785/0120190188.

Lindblom, E., B. Lund, A. Tryggvason, M. Uski, R. Bödvarsson, C. Juhlin, and R. Roberts (2015). Microearthquakes illuminate the deep structure of the endglacial Pärvie fault, northern Sweden, *Geophys. J. Int.* **201,** 1704–1716, doi: 10.1093/gji/ggv112.

Linzer, L. M., M. W. Hildyard, S. M. Spottiswoode, and J. Wesseloo (2019). Do stopes contribute to the seismic source? in *Proc. of the Deep Mining 2019 Conference*, Muldersdrift, 24–25 June 2019, The Southern African Institute of Mining and Metallurgy, 427–444, doi: 10.36487/ACG_rep/1952_32_Linzer.

Linzer, L. M., M. W. Hildyard, and J. Wesseloo (2021). Complexities of underground mining seismic sources, *Phil. Trans. Roy. Soc. London* **379,** doi: 10.1098/rsta.2020.0134.

Lund, B., P. Schmidt, Z. H. Shomali, and M. Roth (2021). The modern Swedish national seismic network: Two decades of intraplate microseismic observation, *Seismol. Res. Lett.* **92,** no 3, 1747–1758, doi: 10.1785/0220200435.

Maceira, M., P. Blom, J. Maccarthy, O. Marcillo, G. Euler, M. Begnaud, S. Ford, M. Pasyanos, G. Orris, M. Foxe, *et al.* (2017). Trends in nuclear explosion monitoring—A physics perspective, *Los Alamos National Laboratory (LA-UR-17-21274)*, doi: 10.2172/1355758.

Malagnini, L., R. B. Herrmann, and M. D. Bona (2000). Ground-motion scaling in the Apennines (Italy), *Bull. Seismol. Soc. Am.* **90,** no. 4, 1062–1081, doi: 10.1785/0119990152.

Manzi, M. S. D., K. A. A. Hein, R. J. Durrheim, and N. King (2014). The Ventersdorp contact reef model in the Kloof gold mine derived from 3D seismic, geological mapping, and exploration borehole data set, *Int. J. Rock Mech. Min. Sci.* **66,** 97–113.

Martinsson, O. (2004). Geology and metallogeny of the Northern Norrbotten Fe-Cu-Au province, in *Svecofennian Ore-Forming Environments: Volcanic-Associated Zn-Cu-Au-Ag, Intrusion-Associated Cu-Au, Sediment-Hosted Pb-Zn, and Magnetite Apatite Deposits in Northern Sweden*, R. L. Allen, O. Martinsson, and P. Weihed (Editors), Vol. 33, Society of Economic Geologists, Littleton, Colorado, 131–148.

Martinsson, O., J. Nordstrand, H. Rutanen, and A. Scott (2013). *Fe oxide and Cu-Au Deposits in the Northern Norrbotten Ore District*, O. Martinsson and C. Wanhainen (Editors), Geological Survey, Sweden, 44–53.

Masethe, R. T. (2022). Integration of 3D seismic data analysis techniques and mining-induced seismic data to elucidate the mechanical behaviour of the rock mass in the gold mines of the Witwatersrand Basin, *Ph.D. Thesis*, University of the Witwatersrand, Johannesburg.

Masethe, R. T., R. J. Durrheim, and M. D. Manzi (2022). Investigation of the source mechanism of mining induced seismic events at Kloof Gold Mine, South Africa, in *Proc. of Tenth International Symposium on Rockbursts and Seismicity in Mines, RaSiM10*, Tucson, Arizona, 26–28 April 2022.

Masethe, R. T., M. D. Manzi, and R. J. Durrheim (2023). Using legacy 3-D seismic data and source parameters of mining induced earthquakes to mitigate the risk of rock bursting in Kloof Gold Mine, South Africa, *Geophys. Pros.* **71,** 1281–1311, doi: 10.1111/1365-2478.13319.

McCarthy, T. S. (2006). The Witwatersrand Supergroup, in *The Geology of South Africa*, M. R. Johnson, C. R. Anhaeusser, and R. J. Thomas (Editors), Geological Society of South Africa, Johannesburg, South Africa, 155–186.

McGarr, A. (1992). An implosive component in the seismic moment tensor of a mining-induced tremor, *Bull. Seismol. Soc. Am.* **19,** 1579–1582.

Mendecki, A. J. (2013). Mine seismology: Glossary of selected terms, in A. Malovichko and D. Malovichko (Editors), *Proc. of Eighth International Symposium on Rockbursts and Seismicity in Mines, RaSiM8*, Geophysical Survey of Russian Academy of Sciences, Mining Institute of Ural Branch of Russian Academy of Sciences, Russia, 527–551.

O'Rourke, C. T., G. E. Baker, and A. F. Sheehan (2016). Using P/S amplitude ratios for seismic discrimination at local distances, *Bull. Seismol. Soc. Am.* **106,** no. 5, 2320–2331.

Pyle, M. L., and W. R. Walter (2019). Investigating the effectiveness of P/S amplitude ratios for local distance event discrimination, *Bull. Seismol. Soc. Am.* **109,** 1071–1081, doi: 10.1785/0120180256.

Sievertsson, Y. (2012). Communities in transformation, *LKAB Magazine*, Vol. 2, 62–67.

Snelson, C., R. Abbott, S. Broome, R. Mellors, H. Patton, A. Sussman, M. Townsend, and W. Walter (2013). Chemical explosion experiments to improve nuclear test monitoring, *Eos Trans. AGU* **94,** 237–239.

Sweby, G., C. Trifu, D. Goodchild, and L. Morris (2006). High resolution seismic monitoring at Mt Keith Open Pit Mine, in *Proc. of Golden Rocks 2006, The 41st U.S. Symposium on Rock Mechanics (USRMS), American Rock Mechanics Association*, Golden, Colorado, 17–21 June 2006, p. 6.

Swedish National Seismic Network (2024). Kiruna region earthquakes, blasts and mining induced events [Data set], Uppsala University, doi: 10.18159/KIR-EBI23

Tankard, A. J., M. P. A. Jackson, K. A. Erickson, O. K. Hobday, D. R. Hunter, and W. E. L. Minter (1982). *Crustal Evolution of Southern Africa: 3.8 Billion Years of Earth History*, Springer, New York.

Taylor, S. R. (1996). Analysis of high-frequency Pg/Lg ratios from NTS explosions and western US earthquakes, *Bull. Seismol. Soc. Am.* **86,** 1042–1053.

Taylor, S. R., A. A. Velasco, H. E. Hartse, W. S. Phillips, W. R. Walter, and A. J. Rodgers (2002). Amplitude corrections for regional seismic discriminants, in *Monitoring the Comprehensive Nuclear-Test-Ban Treaty: Seismic Event Discrimination and Identification*, W. R. Walter and H. E. Hartse (Editors), Vol. 159, Pure and Applied Geophysics, Birkhauser Verlag, Basel, 623–650.

Uski, M., and A. Tuppurainen (1996). A new local magnitude scale for the Finnish seismic network, *Tectonophysics* **261,** 23–37.

Wahlström, R. (1979). Magnitude-scaling of earthquakes in Fennoscandia, *Geophysica* **16,** 51–70.

Walter, W. R., and S. R. Taylor (2001). A revised magnitude and distance amplitude correction (MDAC2) procedure for regional seismic discriminants theory and testing at NTS, *Lawrence Livermore National Laboratory Tech. Rept. UCRL-ID-146882*, doi: 10.2172/15013384.

Walter, W. R., D. A. Dodge, G. Ichinose, S. C Myers, M. E. Pasyanos, and S. R. Ford (2018). Body-wave methods of distinguishing between explosions, collapses, and earthquakes: Application to recent events in North Korea, *Seismol. Res. Lett.* **89,** no. 6, 2131–2138, doi: 10.1785/0220180128.

Walter, W. R., K. M. Mayeda, and H. J. Patton (1995). Phase and spectral ratio discrimination between NTS earthquakes and explosions. Part I: Empirical observations, *Bull. Seismol. Soc. Am.* **85,** 1050–1067.

Wessel, P., J. F. Luis, L. Uieda, R. Scharroo, F. Wobbe, W. H. F. Smith, and D. Tian (2019). The generic mapping tools version 6, *Geochem. Geophys. Geosyst.* **20,** 5556–5564, doi: 10.1029/2019GC008515.

Wesseloo, J., P. Dight, and Y. Potvin (2009). High resolution seismic monitoring in open pit mines, *MERIWA M366 Final Rept. no 279*.

Manuscript received 28 August 2023
Published online 1 March 2024